40th European Rotorcraft Forum
September 2-5,2014, Southampton, United Kingdom
Paper 078

Alleviation of retreating side stall using active elements for helicopter rotors

Vasileios Pastrikakis, René Steijl and George N. Barakos

CFD Laboratory, School of Engineering
University of Liverpool, L69 3GH, U.K.
http://www.liv.ac.uk/flightscience/PROJECTS/CFD/ROTORCRAFT/RBD/index.htm
Email: G.Barakos@liverpool.ac.uk

Abstract

This paper presents CFD results for the performance of the W3-Sokol rotor in forward flight and the potential effect of the implementation of an active Gurney flap. A rigid blade was considered and calculations were conducted based on flight test data. The Gurney flap was extended from 40%R to 65%R and it was located at the trailing edge of the blade. The size of the Gurney was selected to be 2% of the chord based on previous study for the same rotor in hover, and the results were trimmed at the same thrust. The harmonic analysis of the flight test data proved to be a useful tool for identifying vibrations on the rotor caused by Blade Vortex Interaction and stall at the retreating side, and a carefully designed Gurney flap and actuation schedule were essential in order to control the separation of the flow.

NOTATION

GREEK

α	=	Aerofoil lift slope
β	=	Cone angle
θ	=	Collective angle at 75%R
β_c, β_s	=	Flap harmonics
θ_c, θ_s	=	Pitch harmonics
β_0	=	Mean cone angle at 75%R
θ_0	=	Mean collective angle at 75%R
μ	=	Advance ratio
ρ	=	Density, kg/m^3
σ	=	rotor solidity

LATIN

c	=	Chord in untapered part of blade
Q	=	Total moment about shaft axis, Nm
R	=	Aspect ratio of the blade
T	=	Total thrust force, N
V	=	Helicopter speed, Km/h
Re	=	Reynolds Number
M	=	Mach number
C_L	=	Lift coefficient
C_D	=	Drag coefficient
C_M	=	Moment coefficient
C_P	=	Pressure coefficient
F_Z	=	Normal force
F_Y	=	In-plane force
C_T	=	Thrust coefficient, $C_T = \frac{T}{\frac{1}{2}\rho\pi R^2 V_{tip}^2}$
C_Q	=	Torque coefficient, $C_Q = \frac{Q}{\frac{1}{2}\rho\pi R^3 V_{tip}^2}$
FM	=	Figure of merit, $FM = \frac{\sqrt{\sigma}C_T^{\frac{3}{2}}}{2C_Q}$
C_t	=	Sectional thrust coefficient, $C_t = \frac{L_z}{\frac{1}{2}\rho c V_{tip}^2}$
C_m	=	Sectional moment coefficient, $C_m = \frac{L_m}{\frac{1}{2}\rho c^2 V_{tip}^2}$
C_q	=	Sectional torque coefficient, $C_q = \frac{L_q}{\frac{1}{2}\rho c^2 V_{tip}^2}$
L_z	=	Rotor loading along the span in the thrust direction
L_m	=	Rotor moment loading around the blade pitch axis
L_q	=	Rotor moment loading around the shaft axis
CFD	=	Computational Fluid Dynamics
CSD	=	Computational Structure Dynamics
MRB	=	Main Rotor Blade
BVI	=	Blade Vortex Interaction
LDA	=	Laser Doppler Anemometry
VG	=	Vortex generator
SBVG	=	Sub-boundary layer VG
RANS	=	Reynolds Averaged Navier-Stokes
URANS	=	Unsteady RANS
IGE	=	In Ground Effect
OGE	=	Out of Ground Effect

Subscripts

IAS	=	Indicated Aircraft Speed
∞	=	Free-stream Value
tip	=	Tip value

1 INTRODUCTION

Losses due to flow separation are detrimental to rotor performance and normally occur at the retreating side of the rotor where the blade is required to operate at higher angles of attack to balance the rotor disk loads. Retreating blade stall is highly unsteady in nature and the loads produced during stall introduce vibration and make it difficult for the pilot to control the helicopter. Thus, controlling the flow separation is essential. Vortex generators (VG) and Gurney flaps are two flow control devices capable of delaying or alleviating the separation of the boundary layer. The purpose of the study is to compare the possible effect of those devices on curing the dynamic stall occurred during the helicopter forward flight, based on a pitching-translational wing, and then apply the most effective one on the W3 Sokol main rotor blade.

1.1 Vortex Generators

Vortex generators were first introduced by Taylor [1], and ther principle of operation relies on the increased mixing between the external stream and the boundary layer due to longitudinal vortices produced by the VGs. Fluid particles with high momentum in the streamwise direction mix with the low momentum viscous flow inside the boundary layer, thereby, the mean streamwise momentum of the fluid particles in the boundary-layer is increased. The process provides a continuous source of momentum to counter the natural boundary-layer momentum decrease and the growth of its thickness caused by viscous friction and adverse pressure gradients. Vortex generators can reduce or eliminate flow separation in moderate adverse pressure gradient environments. Even when separation does occur for cases of large adverse pressure gradient, the mixing action of trailing vortices will restrict the reversed flow region in the shear layer and help maintain some pressure recovery along the separated flow. Thus the effects of separation may be localised or minimised.

The concept of micro vortex generators was most probably first introduced by Keuthe in the 1970s [2]. In his work, wave-type micro VG with height of 27% and 42% of the boundary layer thickness were installed on an aerofoil to reduce trailing edge noise by suppressing the formation of a Karman vortex street and by reducing the velocity deficit in the aerofoil wake. Since the late 1980s, these devices appeared in the literature under different names such as sub-boundary layer vortex generator (SBVG) [3], submerged vortex generator [4], low-profile vortex generator [5] and micro vortex generator [6].

The major difference between the SBVG and the VG is in terms of the device height. In general, the velocity deficit within a turbulent boundary layer is dominant near the wall within the inner 20% of the boundary layer thickness. It is this region where an adverse external pressure gradient tends to lower the velocity and thus promotes flow separation. Although both devices operate based on a similar mechanism (generation of streamwise vortex), there are some major differences. For example, the SBVG produces a larger velocity gradient close to the wall and has a stronger and lower deficit region in the profile. A vortex generator achieves boundary-layer control only at the penalty of possible considerable drag. A sub-boundary vortex generator produces vortices that travel downstream along the surface, causing flow mixing between the inner layers of the boundary layer. Although these SBVGs will produce extra drag as compared with a clean surface, their drag penalty is less than with VGs.

The wide range of conditions that the rotor is operating makes the parasitic drag a particular limitation, which consists the main drawback of VGs. The only way to avoid this problem is the use of sub-boundary layer VGs as they remain within the low energy flow in the boundary layer and consequently they have low drag. On the other hand, Lin*et al.* [6] [7] used SBVGs on a multi-element aerofoil in a landing configuration and showed that VGs as small as 0.18% of reference wing chord can effectively reduce boundary layer separation on the flap which will lead to reduction of drag and increase of lift for a given angle of attack. In fact during his experimental study trapezoidal vanes were placed on the 25% of the chord of the flap of a wing at flow conditions M=0.2 and $Re = 5 \times 10^6$ creating counter-rotating vortices, and they achieved a 10% lift increase, 50% drag decrease and 100% increase of L/D ratio.

As stated in Kenning's review [8] the potential applications of VGs and SBVGs include control of leading edge separation, shock induced separation and smooth surface separation. SBVGs have less parasitic drag but in case of shock induced separation they must be located closer to the separation line which may be a major limitation in the unsteady application of the rotorcraft. Sub-boundary vortex generators have also been studied at ONERA by Meunier *et al.* [9] as part of AEROMEMS Project in order to control separation on a variable sweep wing. The results of this study show that the efficiency of SBVGs is linked with local boundary thickness which dependents on Reynolds number and angle of incidence.

Ashill et al. [10] also performed a separation control experiment where separation was introduced by placing a bump in the test section. The turbulent boundary layer tunnel was used with a free stream velocity of $40m/s$ and a boundary layer thickness of $40mm$ over the bump. Three types of SBVGs including the micro ramp, micro vane and split micro vane (with a gap $g = 1h$) were tested. All the devices had the same height of $h = 10mm$, resulting in a height ratio of $h/\delta = 0.25$. Laser Doppler anemometry (LDA) was used to perform velocity measurement in streamwise and lateral planes. The velocity fields revealed a significant reduction of the separation region at the rear of the bump for all three devices, furthermore it was found that the split micro vane yielded the best results.

1.2 Gurney flaps

The use of Gurney flaps for lift enhancement is well established in the aerospace community and several research works e.g. [11] document the advantages and disadvantages of these devices. The Gurney flap was introduced by Dan Gurney and its aerodynamics was first studied by [12]. This has been followed by numerous experimental studies [13], [14], and [15]. Tang and Dowell [16] compared the loading of a NACA0012 wing section with both static and oscillating trailing-edge Gurney flaps using an incompressible Navier-Stokes code against experiments conducted in a wind tunnel

by them. Due to the scarcity of experimental data with dynamically deployed Gurney flaps [17], [18], and [19] have utilised this set of data in their computational studies.

The Gurney flap is a short flat plate placed at the trailing edge, perpendicular to the chord-line on the pressure side of the aerofoil, and works by providing a stagnation area near the trailing edge resulting in an increase of lift. It increases the zero lift angle and keeps the lift slope constant so there is a decrease in the stall angle. The pitching moment coefficient is also increased (i.e. more nose down) as presented in [20] and unless the Gurney is sized carefully, substantial drag penalties may also occur. Based on the review of flow control mechanisms [21] Gurney flaps are generally less than 3% of the wing chord. Previous studies [22] and [23] have concluded that the optimal height for a Gurney flap should be close to the boundary layer thickness on the pressure side of the aerofoil. If the Gurney flap height is smaller than the boundary layer thickness, then its influence is significantly decreased, while increasing the size of the flap leads to a drag penalty.

Most of the studies found in the literature are dealing with commonly used aerofoils in rotorcraft applications and try to derive conclusions concerning the potential effect of the Gurney flap on rotor blades according to two-dimensional calculations. Several researchers [24], and [25]. [26] studied the effects of Gurney flaps on the blade root loads and hub vibratory loads. In their study, a Gurney flap was deployed over the entire span of the BO-105 rotor in forward flight with three different deployment schedules. A carefully chosen azimuthal deployment schedule of the Gurney flap was found to reduce the peak-to-peak variations in hub loads. The 4-per-revolution normal force at the hub was compared with the loads for a higher harmonic controlled rotor and the baseline rotor. The simulations showed that the Gurney flap deployment reduced by 80% the 4-per-rev normal force vibration. For the same rotor in descending flight, a Gurney set at 30 degrees angle relative to the mean chord resulted in a 40% decrease of the vertical descend rate. However, the Gurney flap resulted in local nose-down pitching moment, which indicates that additional fluid-structure coupling analysis for aeroelastic deformation is required.

Active Gurney flaps were also studied by Padthe et al. [27] to determine their effectiveness in reducing noise and vibration in rotorcraft, as well as improving rotor performance. Active control studies employing microflaps were conducted on a hingeless rotor configuration resembling the MBB BO-105, and various spanwise configurations of the flaps, including a single, a dual, and a segmented five-flap configuration were evaluated. Results indicate that the Gurney flap is capable of substantial reductions in blade vortex interaction (BVI) noise ranging from 3-6 dB. Vibration reduction ranging from 70-90% was also demonstrated. Vibration and noise reduction was also examined at the same time, and was found that reduction in one was linked to an increase on the other. Finally, the Gurney flap appeared to be more effective in reducing the BVI noise at both advancing and retreating sides while the plain flap was more effective in reducing the vibrations.

The effectiveness of a single active Gurney flap in reducing vibration of a UH-60A Blackhawk helicopter in high-speed flight ($\mu = 0.35$) was studied by Bae and Gandhi [28]. An elastic blade was considered and the Gurney flap was extending from 70%R to 80%R and was deployed to an amplitude of 0.5% of the chord. The Gurney flap actuation was most influential in reducing the vertical vibratory hub force. The most effective actuation input was 4/rev and it led to 80% reduction.

Comparing the above studies [26], [27], and [28], to the ones conducted by Milgram et al. [29], and Viswamurthy and Ganguli [30] it seems that a Gurney flap can have a similar effect on the vibratory loads of the rotor hub like a conventional trailing edge flap. Such a flap is used in [30] on a soft hingeless rotor leading to a 72% reduction of the vibratory loads. However, the advantage of using a Gurney flap compared to a trailing edge flap is on the amount of energy required for the actuation and the ease of the implementation of the Gurney flap.

A further computational study [31] tried to assess active control mechanisms for rotor performance enhancement. A four-bladed rotor was considered at medium $(80kt)$ and high $(150kt)$ speed forward flight cases and the Gurney flap was assumed to be either completely deployed or retracted. A significant increase in thrust for a given power was found when the Gurney was extended from 60%R up to 100%R and activated at the retreating side, which agrees with the outcome of the study by Cheng and Celi [32] who defined the optimum 2-per-revolution inputs in order to improve the rotor performance by either increasing the thrust of the rotor or decreasing the torque requirement. However, the positive effect of the Gurney was observed at medium speed flight while at high speed the performance improvement diminished.

Gagliardi and Barakos [33] studied a low twist hovering rotor and the effects of trailing-edge flaps on its performance. A flap located inboard resulted in hover performance similar to a blade of 6 deg more twist. At the same time, a reduction of the trim angles was observed. A flap located outboard did not improve the performance of the rotor although by carefully optimising its configuration similar trim benefits as for the inboard flap were achieved.

The majority of the previous studies are computational and there is a need for experimental investigations of Gurney flaps on rotors. There is, however, an experimental and computational study of the aeromechanics of a Sikorsky demonstration rotor in [34] that examined the effect of an active flap. The report points out that the Gurney flap may have similar effect to a conventional flap. However, because of its small size the Gurney has the potential for high bandwidth active control with low actuation power requirements and minimal impact to the blade structure when compared to conventional control surfaces.

To conclude, few complete studies concerning Gurney flap implementation on helicopter rotors were found in the literature. All of them investigated the effect of Gurneys on BVI and vibration reduction in forward flight, while Pastrikakis et al. [35] demonstrated the potential effect of Gurney flaps on a hovering rotor. Although there is strong indication from 2D calculations of potential performance enhancement the question still remains whether there is a practical forward flight benefit to be achieved or not. In this work, an active Gurney flap is studied on the main rotor blade of the W3 Sokol helicopter. The enhancement of the performance is investigated

by coupling fluid and structure calculations taking into account the structural properties of the main rotor blade (MRB). The method used for the CFD-CSD coupling was presented in detail in the previous studies of aeroelastic rotors in [36–38]. To the author's knowledge, there are no studies for the effect of the Gurney flap in forward flight with trimmed, aeroelastic methods and CFD for any real rotor blade.

2 NUMERICAL METHOD

2.1 HMB flow solver

The Helicopter Multi-Block 2 (HMB2) CFD code [39], [40], and [41] was employed for this work. HMB2 solves the Navier-Stokes equations in integral form using the arbitrary Lagrangian Eulerian formulation for time-dependent domains with moving boundaries:

$$\frac{\mathrm{d}}{\mathrm{d}t}\int_{V(t)} \vec{w} dV + \int_{\partial V(t)} (\vec{F}_{\mathrm{i}}(\vec{w} - \vec{F}_{\mathrm{v}}(\vec{w})\vec{n} dS = \vec{S}. \qquad (1)$$

The above equations form a system of conservation laws for any time-dependent control volume $V(t)$ with boundary $\partial V(t)$ and outward unit normal $\vec{n}$. The vector of conserved variables is denoted by $\vec{w} = [\rho, \rho u, \rho v, \rho w, \rho E]^T$, where ρ is the density, u, v, w are the Cartesian velocity components and E is the total internal energy per unit mass. $\vec{F}_{\mathrm{i}}$ and $\vec{F}_{\mathrm{v}}$ are the inviscid and viscous fluxes, respectively. For hovering rotors, the grid is fixed, and a source term, $\vec{S} = [0, -\rho\vec{\omega} \times \vec{u}_{\mathrm{h}}, 0]^T$, is added to compensate for the inertial effects of the rotation. $\vec{u}_{\mathrm{h}}$ is the local velocity field in the rotor-fixed frame of reference.

The non-inertial frame of reference used here has two benefits over a rotating frame of reference: (i) the energy equation is unchanged by the rotation vector $\vec{\omega}$ and (ii) a vanishing 'undisturbed' velocity field occurs in contrast to the position-dependent 'undisturbed' velocity field in the rotating frame of reference, which is given by $-\omega \times \vec{r}$.

Equations (1) are discretized using a cell-centred finite volume approach on structured multiblock grids. The spatial discretisation leads to a set of equations in time,

$$\frac{\partial}{\partial t}(\vec{w}_{\mathrm{i,j,k}} V_{\mathrm{i,j,k}}) = -\vec{R}_{\mathrm{i,j,k}}(\vec{w}_{\mathrm{i,j,k}}), \qquad (2)$$

where $\vec{w}$ and $\vec{R}$ are the vectors of cell variables and residuals, respectively. Here, i,j,k are the cells indices in each of the grid blocks, $V_{\mathrm{i,j,k}}$ is the cell volume. The convective terms are discretized using Osher's upwind scheme by [42]. MUSCL variable interpolation is used to provide third-order accuracy and the Van Albada limiter by [43] is employed to prevent spurious oscillations near steep gradients. Boundary conditions are set using ghost cells on the exterior of the computational domain. For viscous flow simulations, ghost values are extrapolated at solid boundaries ensuring that the velocity takes on the solid wall velocity. Implicit time integration is employed, and the resulting linear system of equations is solved using a pre-conditioned Generalised Conjugate Gradient method. For unsteady simulations, an implicit dual-time stepping method is used, based on the pseudo-time integration approach by [44]. The HMB2 method has been validated for a range of rotorcraft applications and has demonstrated good accuracy and efficiency for very demanding flows. Examples of work with HMB2 can be found in references [40], [45], and [41]. Several rotor trimming methods are available in HMB2 along with a blade-actuation algorithm that allows for the near-blade grid quality to be maintained on deforming meshes [40].

The HMB2 solver has a library of turbulence closures including several one- and two- equation turbulence models and even non-Boussinesq versions of the $k - \omega$ model. Turbulence simulation is also possible using either the Large-Eddy or the Detached-Eddy simulation approach. The solver was designed with parallel execution in mind and the MPI library along with a load-balancing algorithm are used to this end. For multi-block grid generation, the ICEM-CFD Hexa commercial meshing tool is used and CFD grids with 40-50 or more million points and thousands of blocks are commonly used with the HMB2 solver.

2.2 Modelling Gurney flaps

For the purposes of this study the effect of the Gurney flap on W3-Sokol MRB is modelled by flagging any block face within the computational mesh occupied by the flap with a solid, no slip boundary condition. This method is implemented in the HMB2 solver and is proved to be simple and effective [46,47]. To be able to obtain the loads on the Gurney flap alone and to be able to find its moment about a different point - for example the Gurney's hinge - HMB2 requires some additional information. Firstly, a special boundary condition tag must be used for the Gurney flap to be identified. Secondly, additional input files must be used to inform HMB2 that computations are to be performed with a Gurney flap. The advantage of this method is that no additional effort is needed in terms of mesh generation. On the other hand, the Gurney is assumed to have no thickness. In case of an actuated Gurney flap a method with overset grids would be required. Otherwise, the deformation of the mesh near the flap would alter the quality of the mesh a lot. Modelling the effect of the flap as stated above allows the mesh quality to remain the same as the mesh do not deforms along with the actuation of the flap.

2.3 Trimming Method

The trimmer used for this study is based on the blade element theory and it is described in [48]. The trimming method consists of an initial trim-state computation and a number of subsequent re-trimming steps. The initial trim state can be obtained either off-line or within the CFD solver. During re-trimming, the collective pitch is updated via a Newton-Raphson process, where the simple aerodynamic model is only used to compute the derivatives of the loads. As a result, upon convergence, the trim state is independent of the approximate aerodynamics. For simulations of forward-flying rotors, re-trimming is carried out after completion of 1 rotor revolution using revolution-averaged integrated loads from CFD solution. The trimming method needs a target thrust coefficient c_{T} as input. In addition models for the fuselage and its drag are necessary in order to compute the total drag, as a function of the advance ratio of the helicopter. From the rotor thrust and total drag, the orientation of the tip-path plane can be obtained, i.e. the forward tilt. For a rotor at straight

level conditions the orientation of the tip-path plane can be obtained from $sin\theta_{\rm tpp} = -D/W$, where D and W represent the total drag of the helicopter and its weight. The aerodynamic model needs an estimate of the induced velocity in the tip-path plane. The induced velocity is assumed constant in the tip-path plane, and is obtained from Glauert's propeller theory [49]. The non dimensional inflow factor λ is defined as

$$\lambda = \frac{Vsin\theta_{\rm tpp} + v_{\rm i}}{\Omega R} = \mu sin\theta_{\rm tpp} + \lambda_{\rm i}, \tag{3}$$

where $v_{\rm i}$ is the induced velocity (<0 for a lifting rotor) and $Vsin\theta_{\rm tpp}$ the inflow due to the rotor disk tilt. In Equation 1, R is the rotor radius and Ω the rotation rate. The inflow factor λ is computed using a Newton-Raphson method to solve the following non-linear equation for $\lambda_{\rm i}$:

$$\lambda_{\rm i} = -\frac{c_{\rm T}}{2}\frac{1}{\sqrt[2]{\mu^2 + (\mu sin\theta_{\rm tpp} + \lambda_{\rm i})^2}}. \tag{4}$$

The collective pitch, cyclic pitch and flapping coefficients can then be calculated. For the collective pitch, the following expression is used [50]:

$$\frac{c_{\rm T}}{\sigma} = \frac{\alpha}{4}[\frac{2}{3}\theta_0\frac{1-\mu^2+9\mu^4/4}{1+3\mu^2/4} + \lambda\frac{1-\mu^2}{1+3\mu^2/4}], \tag{5}$$

where α is the lift slope factor. In equation 3, σ is the solidity of the rotor defined as:

$$\sigma = \frac{N_{\rm blades}c}{\pi R}. \tag{6}$$

With the collective θ_0, the flapping harmonics can be derived from the solution of the blade-flapping equation [50]:

$$\beta_0 = \frac{\gamma}{8}[\theta_0(1+\mu^2) + \frac{4}{3}\lambda - \frac{4}{3}\mu\beta_{\rm 1c}^{\rm (nfp)}], \tag{7}$$

$$\beta_{\rm 1c}^{\rm (nfp)} = \frac{\mu(\frac{8}{3}\theta_0 + 2\lambda)}{1+\frac{3}{2}\mu^2}, \tag{8}$$

$$\beta_{\rm 1s}^{\rm (nfp)} = \frac{\frac{4}{3}\mu\beta_0}{1+\frac{1}{2}\mu^2}, \tag{9}$$

where the subscript (nfp) indicates that the flapping harmonics β_0, $\beta_{\rm 1s}$ are relative to the no-feathering plane, while λ is relative to the tip-path plane. The definition of the no-feathering plane and the relation to the tip-path plane can be found in References [49], [50]. γ is the Lock number and it is defined as

$$\gamma = \frac{\rho\alpha c R^4}{I}, \tag{10}$$

where c is the blade chord and I the moment of inertia about the flap hinge. The present trimming model neglects the lead-lag deflection of the blades, which has only a secondary effect on the rotor blade aerodynamics.

3 W3-SOKOL MRB GEOMETRY

The W3-Sokol main rotor consists of four blades made out of fibre-glass. It is a soft blade in torsion that encourages the idea of the implementation of a Gurney flap in order to alter the twist distribution along the radius of the blade. Fig. 1 presents the geometry of the original MRB. The radius of the blade is along the x-axis and the leading-edge points towards the positive y-axis as the blade is rotating counter-clockwise. Although different sections of 5-digit NACA series are used along the radius, the basic section is the NACA23012M which is created by taking some camber out of the baseline NACA23012. At $0.678R$ of the blade there is a trim tab of $0.1c$ length and $0.07R$ span, while from $0.75R$ and up to the blade tip there is a trailing edge tab of $0.05c$. The tip of the blade is rounded as shown in Fig. 1-III. The MRB has a blunt trailing edge. All these geometrical characteristics increased the complexity of the generated mesh. Adding a fixed Gurney within the multiblock mesh topology would increase the number of nodes and would require additional computational cost to calculate even a steady hover case. For this reason the implementation of a infinitely thin Gurney flap was essential. For forward flight a Gurney flap of $0.02c$ was located at $0.40R$. The span of the Gurney was $0.25R$ and its location and geometry are presented in Fig. 1-I. The Gurney flap was flagged using the local mesh around the blade. This allows a normal to the trailing edge flap of infinite thickness to be simulated. The process is described by [46]. The mesh used for the forward flight calculations consists of 27 million nodes. A mesh convergence study suggested that this large number of cells was needed for the blade-loads to converge. It is a combined C-type topology in the chordwise plane with 402 nodes along the blade and O-type topology in the spanwise plane with 196 nodes around every section of the blade. In the normal direction of the blade 64 nodes have been used. The domain is split in the rotor mesh which includes the rotor blade geometry and the hub, and the background mesh. The flow in the interface of those two meshes is interpolated using sliding planes. The whole domain is split in 5480 blocks and it is presented in Fig. 2.

4 HOVER FLIGHT

This work will complete the study conducted in [35] which demonstrated the potential effect of a Gurney flap on the performance of the W3-Sokol rotor blade in hover. A rigid blade was first considered and the calculations were conducted at several thrust settings. The Gurney flap was extended from 46%R to 66%R and it was located at the trailing edge of the main rotor blade. Four different sizes of Gurney flaps were studied, 2%, 1%, 0.5% and 0.3% of the chord. The biggest flap proved to be the most effective. A second study considered elastic blades with and without the Gurney flap. The results were trimmed at the same thrust values as the rigid blade and indicate an increase of aerodynamic performance when the Gurney flap is used, especially for high thrust cases. Comparative performance calculations have been conducted at six different thrust targets for the rigid clean blade using the $k-\omega$ SST turbulence model. The hover performance for the clean blade as well as the blade with Gurney flaps can be seen in Fig. 3. The maximum FM of the blade did not improve, but at high thrust settings it was enhanced by 6% over the performance of the clean blade. The effect of the Gurney flap to pitch the nose of the section down was evaluated with aeroelastic calculations and it was found that the extra lift of the Gurney in combination with the extra blade twist resulted

in an increased FM.

5 FLIGHT TEST DATA

Data measurements were obtained by PZL-Swidnik for four different flight cases. Hover IGE, forward flight with low, medium, and high speed were considered and 38 different channels were used for measurement tests. Main target of the study was the stall identification. Harmonic analysis was performed for the set of data selected but the stall could only be observed when using the peak to peak values. For that reason, a new set of data was received for forward flight at indicated speed between 236 km/h and 245 km/h, while at the same time the weight of the helicopter was the maximum allowed weight according to the design specifications (6400 kg). The time domain flight parameters for that case are presented in Fig. 4. As a result the stall was more severe and could easily be identified. Fig. 5 presents the peak to peak values for the torsional moment, and the flapping bending moment at r=0.23R. Fig. 6 presents the harmonic analysis for the flap, lag and feather angles of the first blade. Based on previous flight test data processing, for a four bladed rotor the existence of high harmonic content frequencies which can not be divided by 4 indicates vibrations due to stall.

Based on the stall evidence the trim state of the main rotor that should be used in forward flight calculations, as well as the flow conditions were decided. Table 1 presents the forward flight conditions of the W3 rotor.

6 COMPARISON OF GURNEY FLAP AND VORTEX GENERATORS

Before running the forward flight calculation for the W3 Sokol main rotor, a comparative study was conducted regarding the potential effect of the Gurney flaps and the vortex generators on stall alleviation. First static calculations were run for a clean wing NACA23012M of 1.15c span with 2D symmetry conditions applied on the boundaries. Then Gurney flaps of different sizes located at the trailing edge, as well as an array of counter rotating vortex generators of different sizes located at 20% of the chord were used along the whole span of the wing. The results are presented in Figs. 7,8 and indicate that although the additional drag and the pitching down moments introduced by the Gurney flap are an important limitation at high angles of attack, a carefully design actuation schedule of the Gurney flap can result in the same positive effect that the vortex generators have at high angle of attack, while at the same time the very important positive effect compared to the vortex generators at low angles of attack will be maintained. This will result at higher L/D ratio and the performance of the wing will be improved.

In order to evaluate the effect of the above flow control devices on preventing or delaying the separation of the flow due to dynamic stall several dMdt calculations were conducted next. A dMdt is an unsteady calculation where an aerofoil or a wing is set to a pitching and translational oscillative motion so that the forward flight effect on a rotor blade section can be simulated. The harmonic motion of the wing is given by:

$$x = x_0 + \sum_{i=1}^{nhar} x_s sin(2kit) + x_c cos(2kit), \qquad (11)$$

where the x_0 is the mean translation, $nhar$ is the number of harmonics, k is the reduced frequency of the first harmonic, and x_s and x_c are the coefficients of the sine and cosine contribution of each harmonic.

At this study a NACA23012M section with 4 chords span was used again with 2D symmetry conditions applied on the boundaries, while the pitch and translational schedule were selected based on flight test data of the W3 Sokol helicopter so that the wing experiences dynamic stall. On a forward flight case of freestream speed $M_\infty = 0.2052$ a blade section experiences a flow due to rotation, which is constant around the azimuth Ψ, and due to the translation of the helicopter. The overall local speed is equal to:

$$M_{section} = M_{tip}\frac{r}{R} + M_\infty sin(\Psi). \qquad (12)$$

The parameters that are used in the calculation are presented in Table 2, while Fig. 9 presents the pitch, and the translation that the wing section experiences, as well as the local velocity of the wing. Although the inflow effect is not taken into account dMdt is a very good and cheap calculation compared to a rotor case in order to approximate the forward flight effect on a blade section of a rotor.

Figs. 10,12,13 as well as Table 3 present the loads on the wing with and without the flow control devices and shows that specific pitch and translational schedule of the wing where a small indication of stall was observed the active Gurney flap resulted in a slightly better performance and it increased the L/D ratio at the retreating side ($\Psi = 270^o$). Thus, after the identification of stall on the W3 Sokol main rotor an active Gurney flap will be used to delay or alleviate the the separation of the flow.

7 FORWARD FLIGHT

The flow conditions of the rigid rotor in forward flight were based on the flight test data. It was a high advance ratio flight ($\mu = 0.3229$), the freestream speed was $M = 0.2052$, and the Reynolds number based on that speed and the blade root chord was $Re = 1.2 \times 10^6$. Fig. 14 presents the schedule of the feathering angle and the flapping angle of the blade around the azimuth. Based on that schedule the blade seems to operate beyond to the stall limit of the NACA23012M aerofoil at the retreating side, which could be the cause for stalling at the inboard sections. The $k-\omega$ SST turbulence model was used and the rotor completed 4 revolutions with quarter degree steps before the loads reached convergence. A separated flow region was identified at the retreating side of the rotor as expected. Fig. 15 presents the pressure distribution at 45% of the blade radius at several azimuthal positions between $\Psi = 210^o$ and $\Psi = 310^o$. The pressure has already started to diverge at $\Psi = 225^o$, which indicates the stall onset, while the flow is reattached at $\Psi = 300^o$. Fig. 16 also presents the separated flow using streamlines at $\Psi = 270^o$. After proccessing the CFD results Fig. 17 presents the stall map along with the designed actuation algorithm of the Gurney flap which had a span of 0.25R and its size was 0.02c

based on the performance on the flap at the same rotor in hover. Figs. 18,19,20 present a comparison of the pressure distribution between the clean rotor and the rotor with the active Gurney in inboard sections of the blade at the retreating side. It is observed that the effect of the Gurney flap decays rapidly away from the tips as well as that the pressure coefficient diverges less when the Gurney flap is actuated which indicates that the flap has taken out some of the stall. Figs. 21,22 present the disk loads for the clean rotor and the rotor with the active flap respectively pointing out the higher lift capability of the retreating side of the rotor when the Gurney is actuated as well as the strong pitching down moments introduced. Moreover, Fig. 23 presents the pressure coefficient distribution on the blade at both cases based on the freestream velocity and the effect of the Gurney on decreasing the pressure on the suction side of the blade. In order to obtain more indicative results regarding the Gurney effect on reducing the separation both cases were trimmed at the same thrust settings. Fig. 24 presents the trimming history of the computations. For the case where the Gurney was actuated the torque requirement of rotor was decreased by 2% which corresponds to $25KW$. Fig. 25 presents once more the streamlines on separation region of the blade at $\Psi = 270^o$ along with the effect of the Gurney flap. The blade of Fig. 25b is pitched down and the flow is less separated compared to the clean case.

8 Conclusions and Future Work

In this work the use of a Gurney flap was put forward to improve the forward flight performance of a helicopter rotor by reducing the stall at the retreating side. The basic idea is that the flap will be actively actuated in forward flight and will be fully deployed in hover flight. The W3 Sokol MRB was used due to the availability of flight test data as well as the blade shape and structural properties. A carefully designed Gurney flap and actuation schedule proved to be essential in order to control the separation of the flow for the rigid blade computations. In the future, further computations will be run considering an elastic blade as for a soft blade in torsion coupling of CFD and CSD is important for the study of the W3 Sokol at high speed.

Acknowledgements
The financial support via the IMESCON Marie Curie ITN project (grant agreement number: 264672), the release of the W3 Sokol main rotor blade geometry by PZL Swidnik, and the use of the computing centre TASK of Gdansk, Poland, are gratefully acknowledged.

References

[1] H. D. Taylor, "The elimination of diffuser separation by vortex generators," *United Aircraft Corporation Report*, vol. R-4012-3, pp. East Hartford, CT, 1947.

[2] A. M. Keuthe, "Effect of streamwise vortices on wake properties associated with sound generation," *Journal of Aircraft*, vol. 10, pp. 715–719, 1972.

[3] A. E. Holmes, P. K. Hickey, W. R. Murphy, and D. A. Hilton, "The application of sub-boundary layer vortex generators to reduce canopy "Mach rumble" interior noise on the gulfstream iii," *AIAA paper*, vol. 84, 1987.

[4] J. R. Rao, "Boundary-layer submerged vortex generators for separation control - an exploratory study," *AIAA paper - 3546*, 1988.

[5] D. C. McCormick, "Shock/boundary-layer interaction control with vortex generators and passive cavity," *AIAA paper*, vol. 31, pp. 91–96, 1993.

[6] J. C. Lin, S. K. Robinson, R. J. McGhee, and W. O. Valarezo, "Separation control on high-lift airfoils via micro-vortex generators," *Journal of Aircraft*, vol. 31, no. 6, pp. 1317–1323, 1994.

[7] J. C. Lin, "Review of research on low-profile vortex generators to control boundary-layer separation," *Progress in Aerospace Sciences*, vol. 38, no. 4-5, pp. 389–420, 2002.

[8] O.C.Kenning, I.W.Kaynes, and J.V.Miller, "The potential application of flow control to helicopter rotor blades)," in *30th European Rotorcraft Forum*, 2004.

[9] M. Meunier and V. Brunet, "High-lift devices performance enhancement using mechanical and air-jet vortex generators," *Journal of Aircraft*, vol. 45, no. 6, pp. 2049–2061, 2008. Cited By (since 1996): 3.

[10] P. R. Ashill, J. L. Fulker, and K. C. Hackett, "Research at DERA on sub boundary layer vortex generators (SBVGs)," in *39th Aerospace Sciences Meeting and Exhibit*, 2001.

[11] J. J. Wang, Y. C. Li, and K. S. Choi, "Gurney flap - Lift enhancement, mechanisms and applications," *Progress in Aerospace Sciences*, vol. 44, pp. 22–47, 2008.

[12] R. H. Liebeck, "Design of subsonic airfoils for high lift," *Journal of Aircraft*, vol. 15, pp. 547–561, Sept 1978.

[13] D. Jeffrey and X. Zghang, "Aerodynamics of Gurney Flaps on a Single-Element High-Lift Wing," *Journal of Aircraft*, vol. 37, pp. 295–301, March-April 2000.

[14] D. R. Troolin, E. K. Longmire, and W. T. Lai, "Time Resolved PIV Analysis of Flow over a NACA 0015 Airfoil with Gurney Flap," *Experiments in Fluids*, vol. 41, pp. 241–254, 2006.

[15] T. Lee and Y. Y. Su, "Lift Enhancement and Flow Structure of Airfoil with Joint Trailing-Edge Flap and Gurney Flap," *Experiments in Fluids*, vol. 50, pp. 1671–1684, 2011.

[16] D. Tang and E. H. Dowell, "Aerodynamic Loading for an Airfoil with an Oscillating Gurney Flap," *Journal of Aircraft*, vol. 44, pp. 1245–1257, July-August 2007.

[17] R. Chow and C. P. V. Dam, "Unsteady computational investigations of deploying load control microtabs," *Journal of Aircraft*, vol. 43, pp. 1458–1469, Sept–Oct 2006.

[18] J. P. Baker, K. J. Standish, and C. P. van Dam, "Two-dimensional wind tunnel and computational investigation of a microtab modified airfoil," *Journal of Aircraft*, vol. 44, pp. 563–572, March-April 2007.

[19] M. P. Kinzel, M. D. Maughmer, and E. P. N. Duque, "Numerical investigation on the aerodynamics of oscillating airfoils with deployable gurney flaps," *AIAA Journal*, vol. 48, pp. 1457–1469, July 2010.

[20] S. L. Gai and R. Palfrey, "Influence of trailing-edge flow control on airfoil performance," *Journal of Aircraft*, vol. 40, no. 2, pp. 332–337, 2003.

[21] H. Yeo, "Assessment of active controls for rotor performance enhancement," *Journal of the American Helicopter Society*, vol. 53, no. 2, pp. 152–163, 2008.

[22] D. Jeffrey, X. Zhang, and D. W. Hurst, "Aerodynamics of gurney flaps on a single-element high-lift wing," *Journal of Aircraft*, vol. 37, no. 2, pp. 295–301, 2000.

[23] M. D. Maughmer and G. Bramesfeld, "Experimental investigation of gurney flaps," *Journal of Aircraft*, vol. 45, no. 6, pp. 2062–2067, 2008.

[24] K. Yee, W. Joo, and D. H. Lee, "Aerodynamic performance analysis of a gurney flap for rotorcraft applications," *Journal of Aircraft*, vol. 44, pp. 1003–1014, May–June 2007.

[25] L. Liu, A. K. Padthe, and P. P. Friedmann, "Computational study of microflaps with application to vibration reduction in helicopter rotors," *AIAA Journal*, vol. 49, pp. 1450–1465, July 2011.

[26] B. Min, L. N. Sankar, N. Rajmohan, and J. V. R. Prasad, "Computational investigation of gurney flap effects on rotors in forward flight," *Journal of Aircraft*, vol. 46, no. 6, pp. 1957–1964, 2009.

[27] A. K. Padthe, L. Liu, and P. P. Friedmann, "Numerical Evaluation of Microflaps for on Blade Control of Noise and Vibration," in *Collection of Technical Papers - AIAA/ASME/ASCE/AHS/ASC Structures, Structural Dynamics and Materials Conference*, 2011.

[28] E. S. Bae and F. Gandhi, "Upstream active gurney flap for rotorcraft vibration reduction," in *Annual Forum Proceedings - AHS International, 1–3 May 2012, Texas, USA*, vol. 2, pp. 1354–1362.

[29] J. Milgram, I. Chopra, and F. Straub, "Rotors with trailing edge flaps: Analysis and comparison with experimental data," *Journal of the American Helicopter Society*, vol. 43, no. 4, pp. 319–332, 1998.

[30] S. R. Viswamurthy and R. Ganguli, "An optimization approach to vibration reduction in helicopter rotors with multiple active trailing edge flaps," *Aerospace Science and Technology*, vol. 8, no. 3, pp. 185–194, 2004.

[31] H. Yeo, "Assessment of active controls for rotor performance enhancement," in *Annual Forum Proceedings - AHS International, May 9–11 2006, Phoenix, USA*, vol. 2, pp. 935–953.

[32] R. P. Cheng and R. Celi, "Optimum two-per-revolution inputs for improved rotor performance," *Journal of Aircraft*, vol. 42, no. 6, pp. 1409–1417, 2005.

[33] A. Gagliardi and G. N. Barakos, "Analysis and design of a flap-equipped low-twist rotor for hover," *Journal of Aircraft*, vol. 46, no. 1, pp. 74–84, 2009.

[34] P. Lorber, B. Hein, J. Wong, and B. Wake, "Rotor aeromechanics results from the sikorsky active flap demonstration rotor," in *Annual Forum Proceedings - AHS International*, vol. 1, pp. 553–568, 2012.

[35] V. P. Pastrikakis, R. Steijl, and G. N. Barakos, "Computational aeroelastic analysis of a hovering w3 sokol blade with gurney flap," *Journal of Fluids and Structures*, no. 1763, 2014.

[36] F. Dehaeze and G. N. Barakos, "Hovering rotor computations using an aeroelastic blade model," *Aeronautical Journal*, vol. 116, no. 1180, pp. 621–649, 2012.

[37] F. Dehaeze and G. N. Barakos, "Mesh deformation method for rotor flows," *Journal of Aircraft*, vol. 49, no. 1, pp. 82–92, 2012.

[38] F. Dehaeze and G. N. Barakos, "Aeroelastic cfd computations for rotor flows," in *37th European Rotorcraft Forum 2011*, pp. 143–162, 2011.

[39] G. Barakos, R. Steijl, K. Badcock, and A. Brocklehurst, "Development of CFD Capability for Full Helicopter Engineering Analysis.." 31st European Rotorcraft Forum, 13-15 September 2005, Florence, Italy, 2005.

[40] R. Steijl, G. Barakos, and K. Badcock, "A framework for CFD analysis of helicopter rotors in hover and forward flight," *International Journal for Numerical Methods in Fluids*, vol. 51, no. 8, pp. 819–847, 2006.

[41] R. Steijl and G. Barakos, "Sliding Mesh Algorithm for CFD Analysis of Helicopter Rotor-Fuselage Aerodynamics," *International Journal for Numerical Methods in Fluids*, vol. 58, pp. 527–549, 2008.

[42] S. Osher and S. Chakravarthy, "Upwind schemes and boundary conditions with applications to euler equationsin general geometries," *Journal of Computational Physics*, no. 50, pp. 447–481, 1983.

[43] G. D. V. Albada, B. V. Leer, and W. Roberts, "A comparative study of computational methods in cosmic gas dynamics," *Astron. Astrophysics*, vol. 108, p. 76, 1982.

[44] A. Jameson, "Time Dependent Calculations Using Multigrid, with Applications to Unsteady Flows Past Airfoils and Wings," in *10th Computational Fluid Dynamics Conference, Honolulu, HI*, 1991. AIAA-91-1596.

[45] R. Steijl and G. Barakos, "A Computational Study of the Advancing Side Lift Phase Problem," *Journal of Aircraft*, vol. 45, no. 1, pp. 246–257, 2008.

[46] M. Woodgate and G. N. Barakos, "Rotor computations with active gurney flaps," *38th European Rotorcraft Forum, September 4–7, Amsterdam, Netherlands*, no. 54, 2012.

[47] M. Woodgate, V. Pastrikakis, and G. N. Barakos, "Rotor computations with active gurney flaps," ERCOFTAC international symposium "Unsteady separation in fluid-structure interaction", Mykonos, Greece, June 2013.

[48] R. Steijl, G. Barakos, and K. Badcock, "A framework for cfd analysis of helicopter rotors in hover and forward flight," *International Journal for Numerical Methods in Fluids*, vol. 51, pp. 819–847, July 2006.

[49] S. Newman, "The foundations of helicopter flight," *Edward Arnold: London, 1994*.

[50] J. Seddon, "Basic helicopter aerodynamics," *BSP Professional Books: Oxford, 1990*.

Flight Parameters	
V_{IAS}	$244.4Km/h$
M_∞	0.2052
Re_∞	1.2x10^6
μ	0.3229
θ_0	$12.38deg$
β_0	$3.55deg$
θ_c	$-4.87deg$
θ_s	$8.68deg$
β_c	$-1deg$
β_s	$-3.5deg$

Table 1: Forward flight conditions for the W3 Sokol main rotor.

Parameters	**Value**
μ	0.3229
reduced frequency	0.06228
mean rotation	10.0 deg.
θ_c	-2.0 deg
θ_s	4.0 deg
mean translation	0.0 c
β_c	-4.9627 c
β_s	0.0

Table 2: dMdt parameters used for NACA23012M wing with active Gurney flap and vortex generators.

Case	M^2C_L	M^2C_D	M^2C_M	L/D
Clean wing	2.56×10^{-2}	0.60×10^{-2}	0.320×10^{-3}	4.305
Wing with active gurney flap	2.77×10^{-1}	0.64×10^{-2}	-0.046×10^{-3}	4.350
Wing with vortex generators	2.57×10^{-2}	0.60×10^{-2}	0.319×10^{-3}	4.295

Table 3: Loads for clean wing and wing with flow control devices at azimuth $\Psi = 270^o$ during dMdt computations.

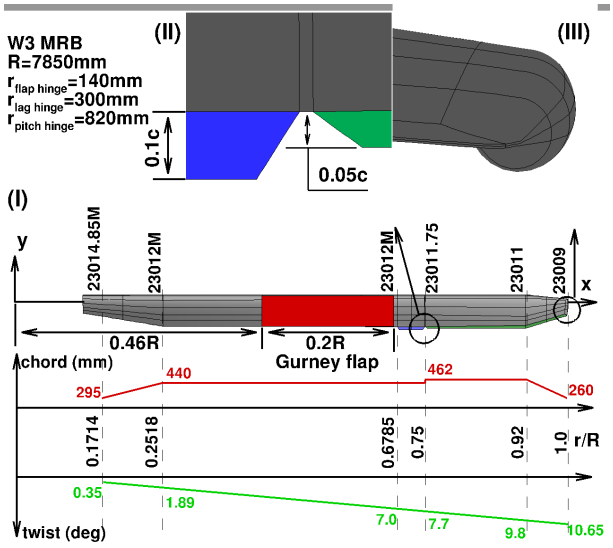

Figure 1: (I) Geometry of W3-Sokol MRB, (II) close view at the trim tab and the trailing edge tab, (III) close view at the tip.

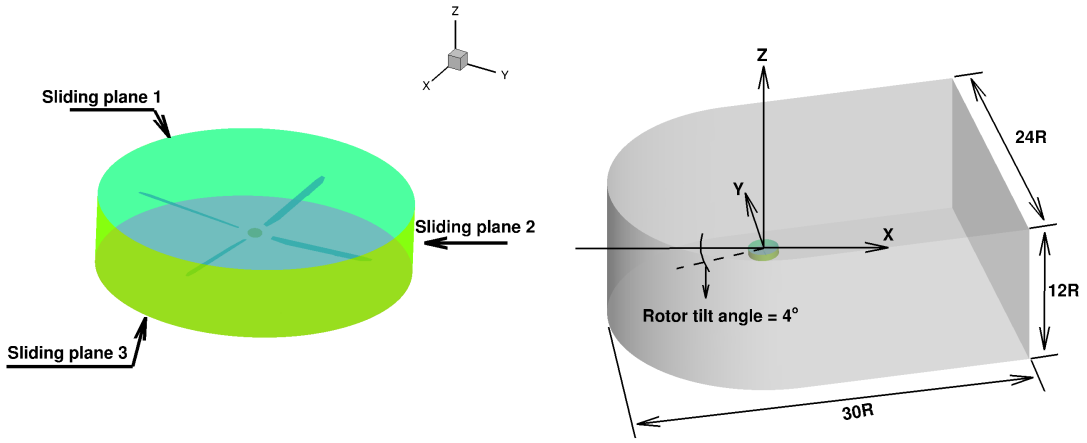

(a) (b)

Figure 2: (a) Sliding planes around W3 MR in forward flight, and (b) overview of the computational domain used for the forward flight calculations.

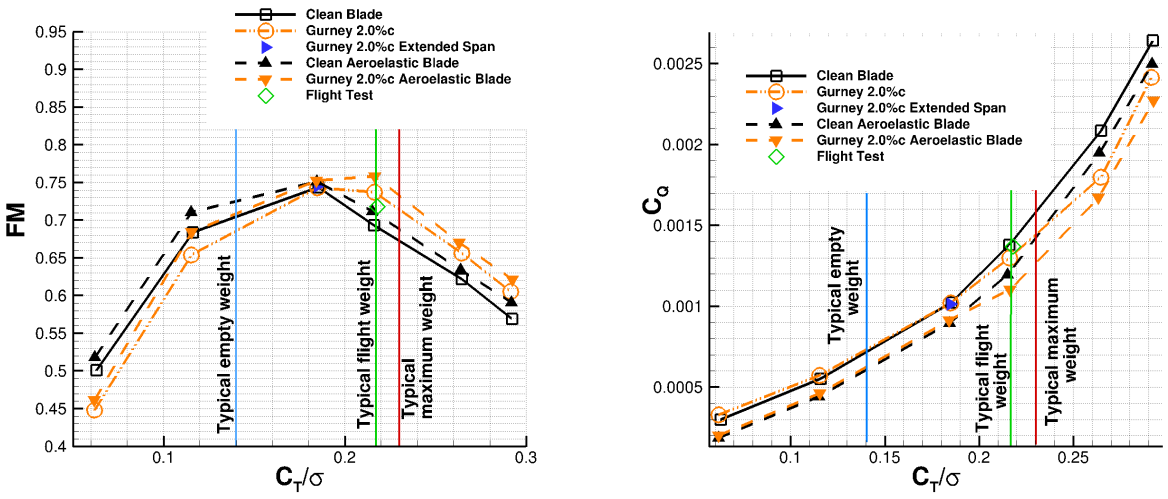

(a) (b)

Figure 3: (a) Figure of merit, and (b) torque coefficient versus thrust coefficient for the W3 Sokol MR blade in hover ($M_{\text{tip}} = 0.618, \text{Re}_{\text{tip}} = 3.74 \cdot 10^6, \sigma = 0.0714$).

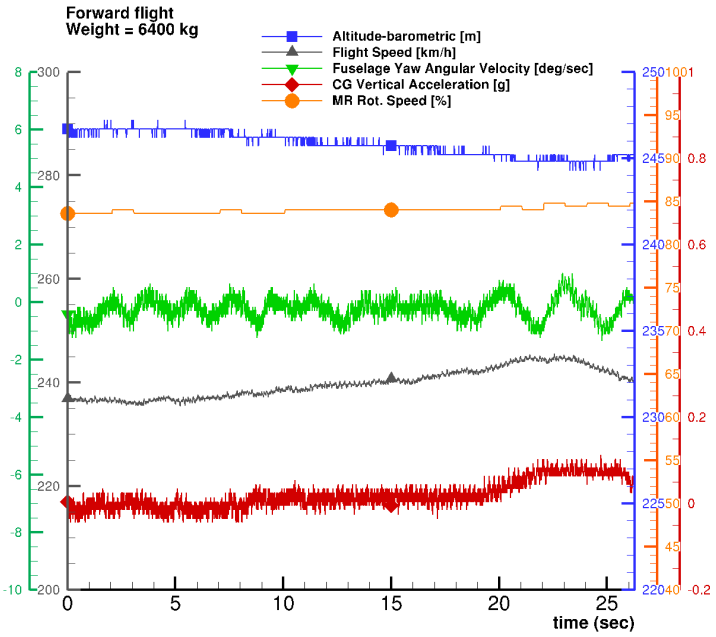

Figure 4: Time domain flight parameters for forward flight with helicopter weight equals to 6400 kg.

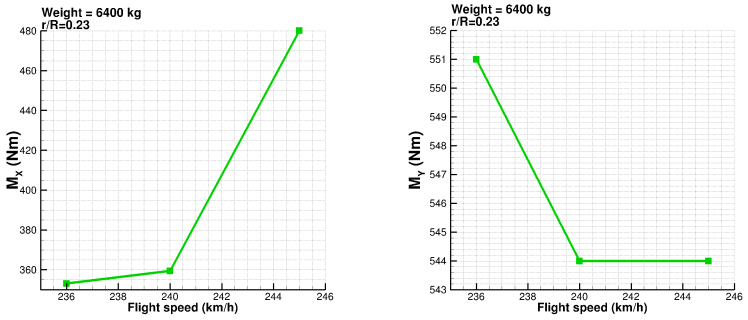

(a) (b)

Figure 5: Peak to peak values of (a) torsional moment, and (b) flapping bending moment at r/R=0.23, helicopter weight equals to 6400 Kg.

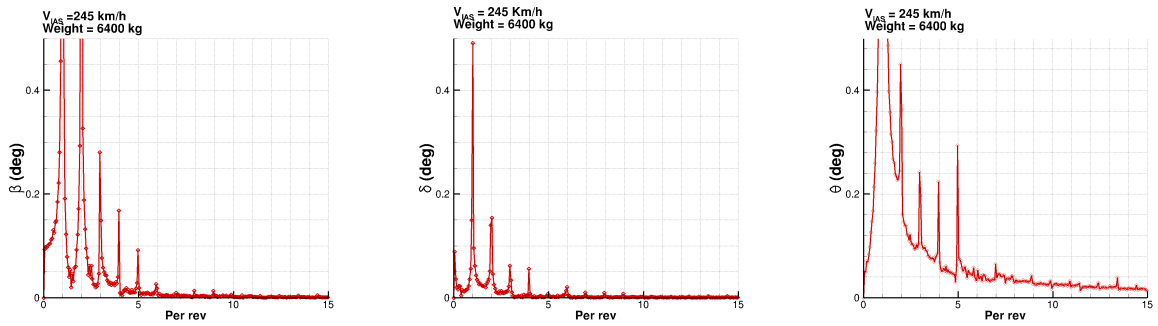

(a) (b) (c)

Figure 6: Harmonic analysis of (a) flapping angle, (b) lagging angle, and (c) feathering angle of the first MR blade, helicopter weight equals to 6400 Kg.

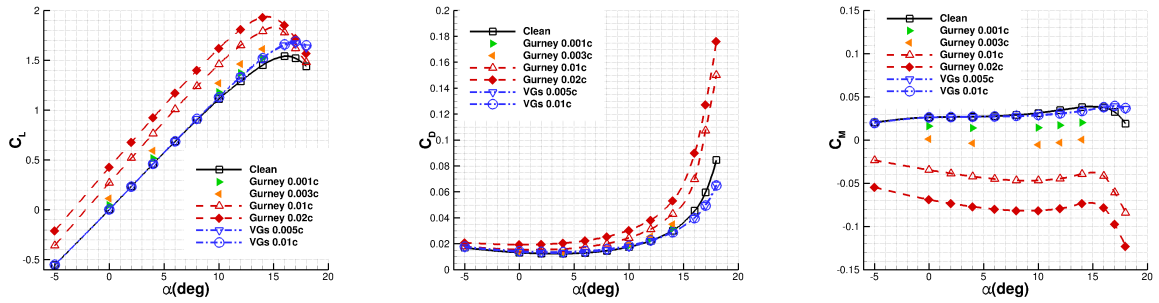

(a) (b) (c)

Figure 7: (a) Lift, (b) drag, and (c) moment coefficients for a wing NACA23012M. dMdt case is presented in Table 2.

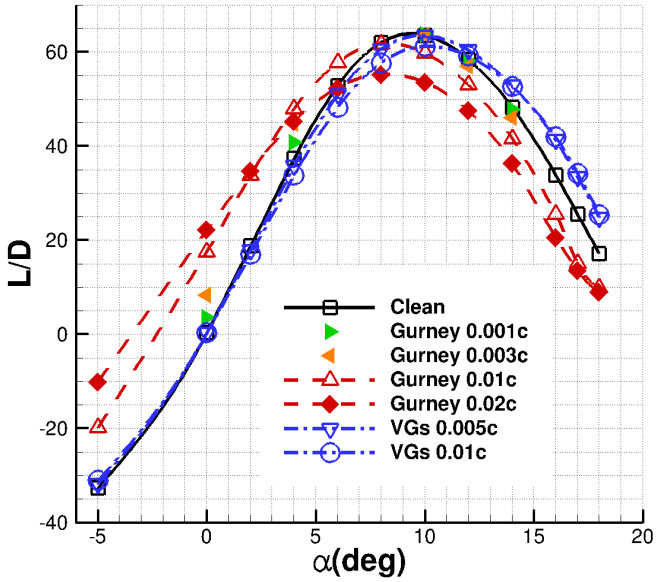

Figure 8: Lift over drag ratio comparison between gurney flaps and vortex generators for a wing NACA23012M. dMdt case is presented in Table 2.

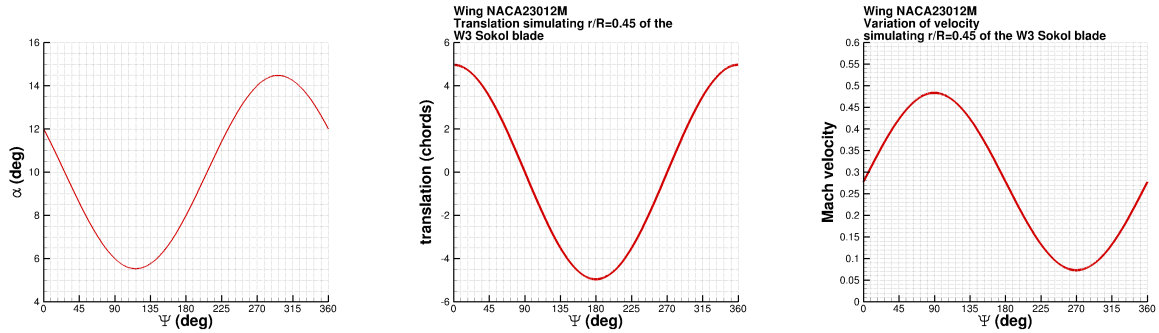

(a) (b) (c)

Figure 9: (a) Pitching, (b) translational motion, and (c) variation of the local velocity of the NACA23012M wing. dMdt case is presented in Table 2.

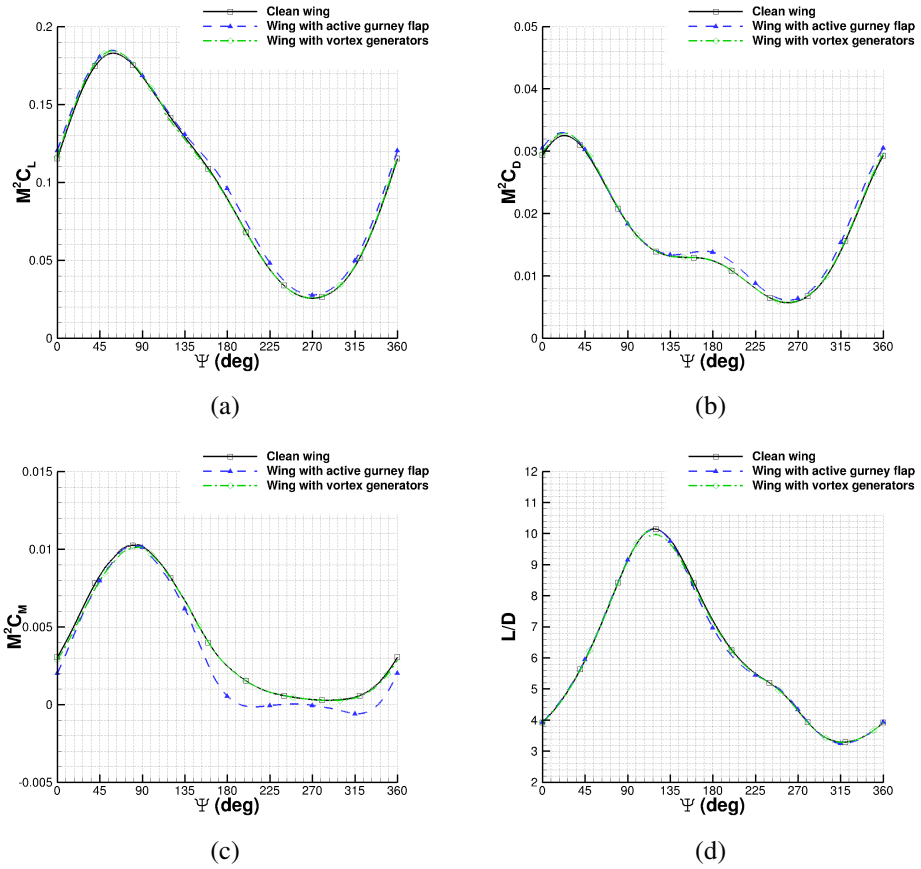

Figure 10: (a) M^2C_L, (b) M^2C_D, (c) M^2C_M, and (d) L/D comparison for clean wing (black solid line), wing with active gurney flap (blue dashed line), and wing with vortex generators (green dashed-dotted line). dMdt case is presented in Table 2.

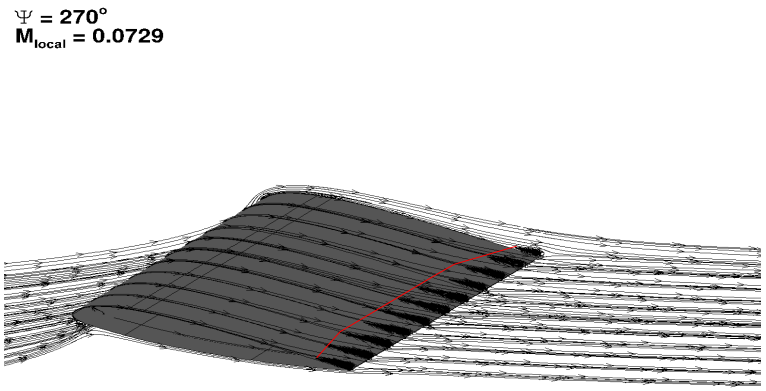

Figure 11: Visualization of the streamlines along the span of the clean wing. The red line indicates the onset of the separation. dMdt case is presented in Table 2.

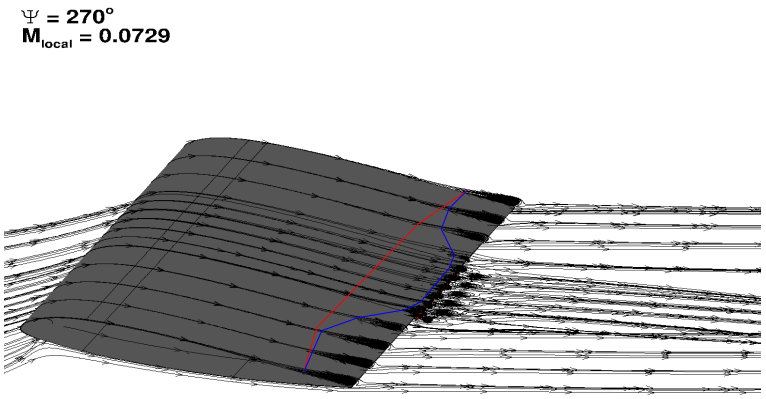

Figure 12: Visualization of the streamlines along the span of the wing with active gurney flap. The red and blue line indicates the onset of the separation for the clean wing and the wing with active gurney respectively. dMdt case is presented in Table 2.

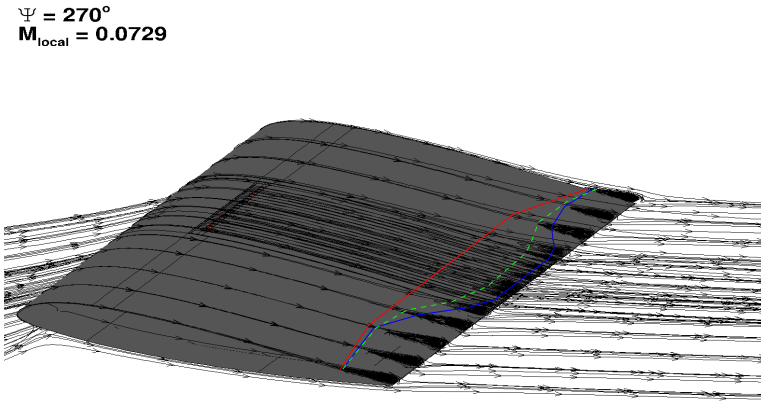

Figure 13: Visualization of the streamlines along the span of the wing with vortex generators. The dashed green line indicates the onset of the separation for the wing with the vortex generators. dMdt case is presented in Table 2.

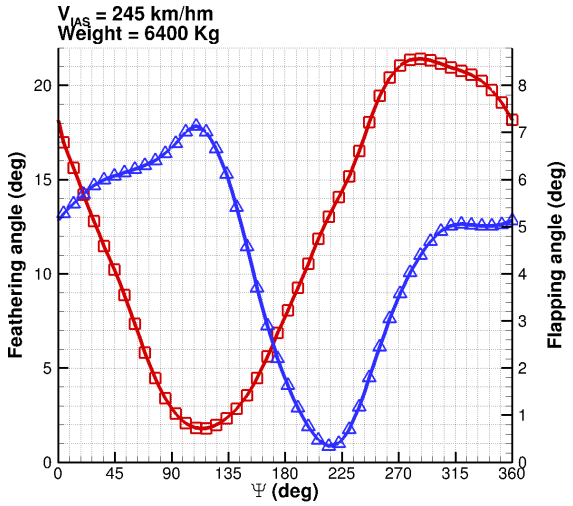

Figure 14: Schedule for the feathering and flapping angle for the W3 Sokol MR blade in forward flight. Case conditions are presented in Table 1.

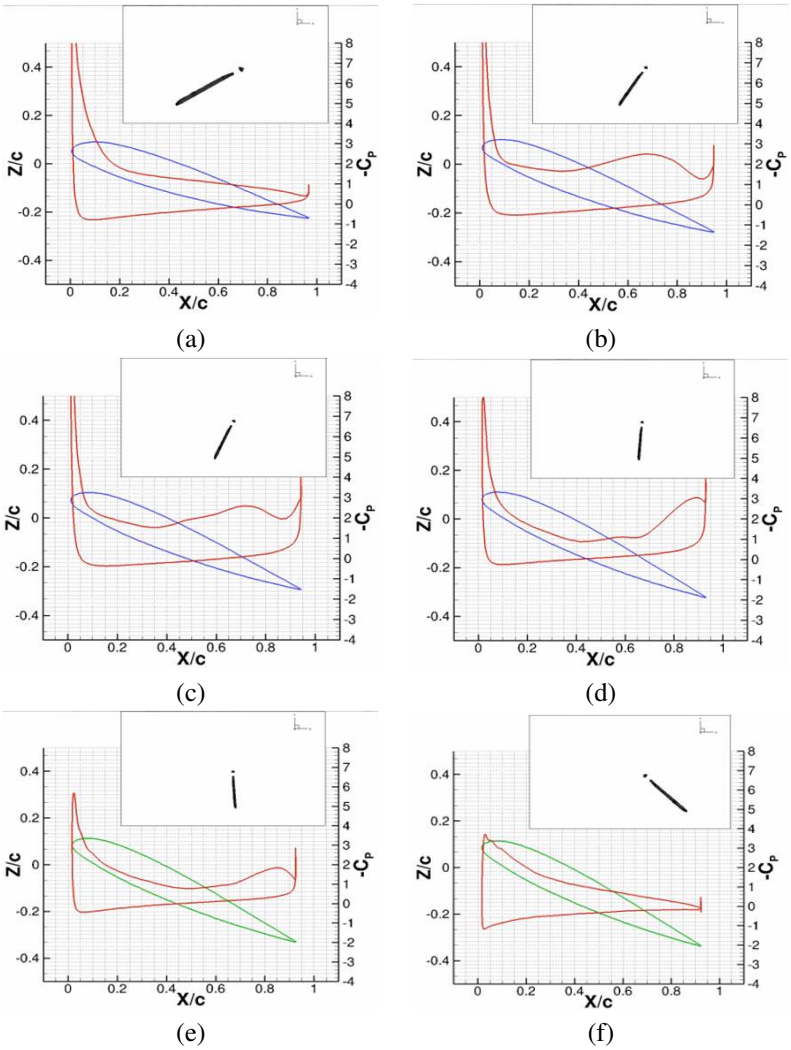

Figure 15: Pressure distribution at $r/R = 0.45$ of the W3 Sokol blade in forward flight at (a) $\Psi = 210^o$, (b) $\Psi = 225^o$, (c) $\Psi = 250^o$, (d) $\Psi = 265^o$, (e) $\Psi = 280^o$, and (f) $\Psi = 310^o$. Case conditions are presented in Table 1.

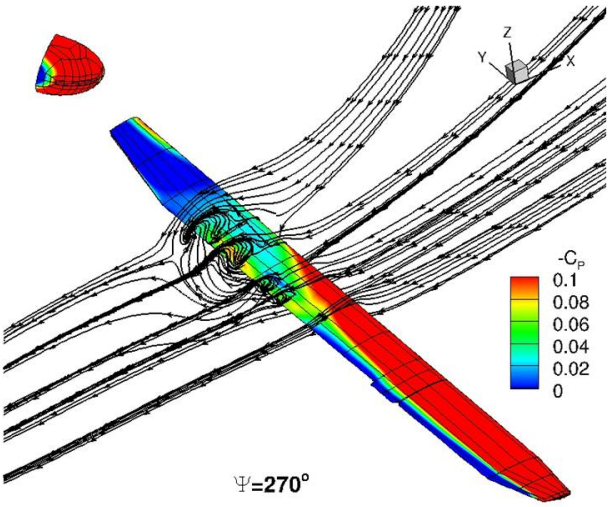

Figure 16: Streamlines visualization on the W3 Sokol MRB in forward flight at $\Psi = 210^o$. Case conditions are presented in Table 1.

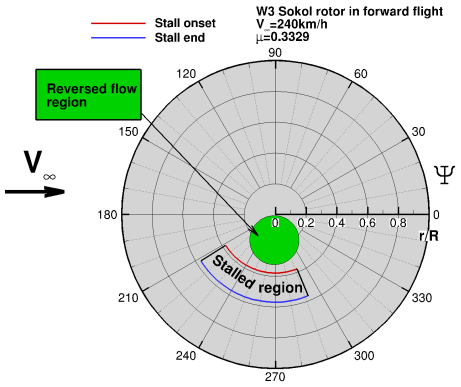

(a)

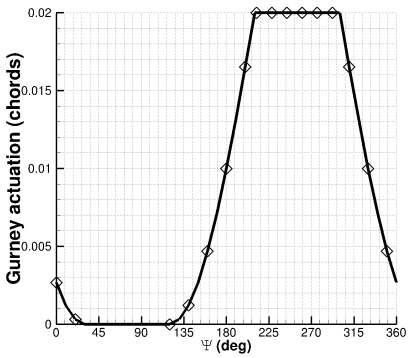

(b)

Figure 17: (a) Stall map of W3 Sokol blade in forward flight, and (b) actuation schedule of gurney flap. Case conditions are presented in Table 1.

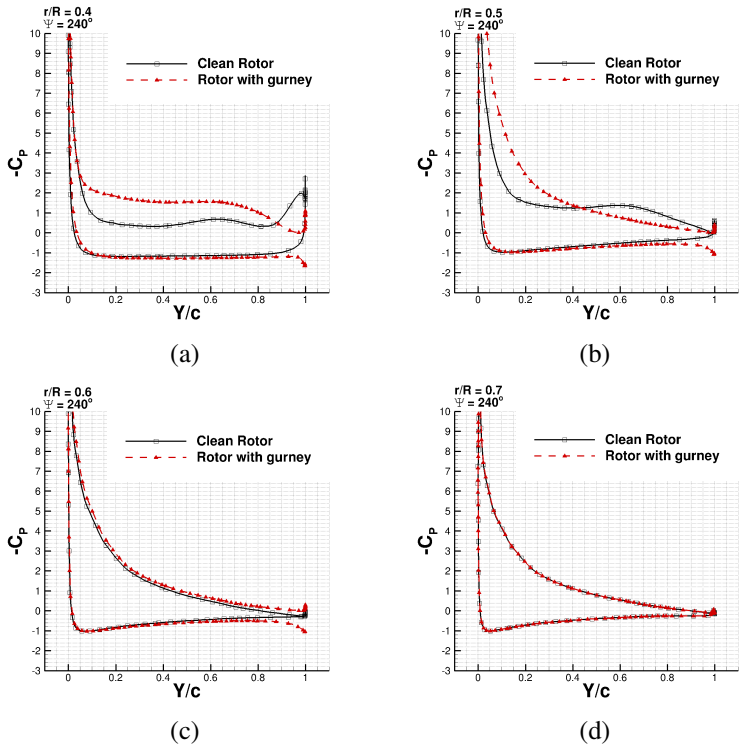

Figure 18: Surface pressure coefficient at $r/R = 0.4$ (a), $r/R = 0.5$ (b), $r/R = 0.6$ (c), and $r/R = 0.7$ (d) of the approximate W3 Sokol blade at azimuth $\Psi = 240^o$ at forward flight. Forward flight conditions are presented in Table 1.

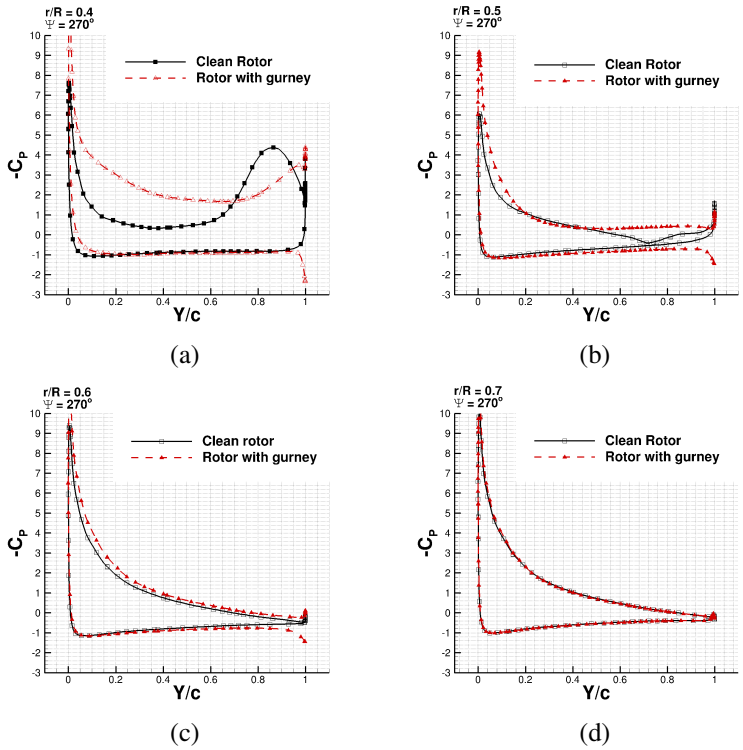

Figure 19: Surface pressure coefficient at $r/R = 0.4$ (a), $r/R = 0.5$ (b), $r/R = 0.6$ (c), and $r/R = 0.7$ (d) of the approximate W3 Sokol blade at azimuth $\Psi = 270^o$ at forward flight. Case conditions are presented in Table 1.

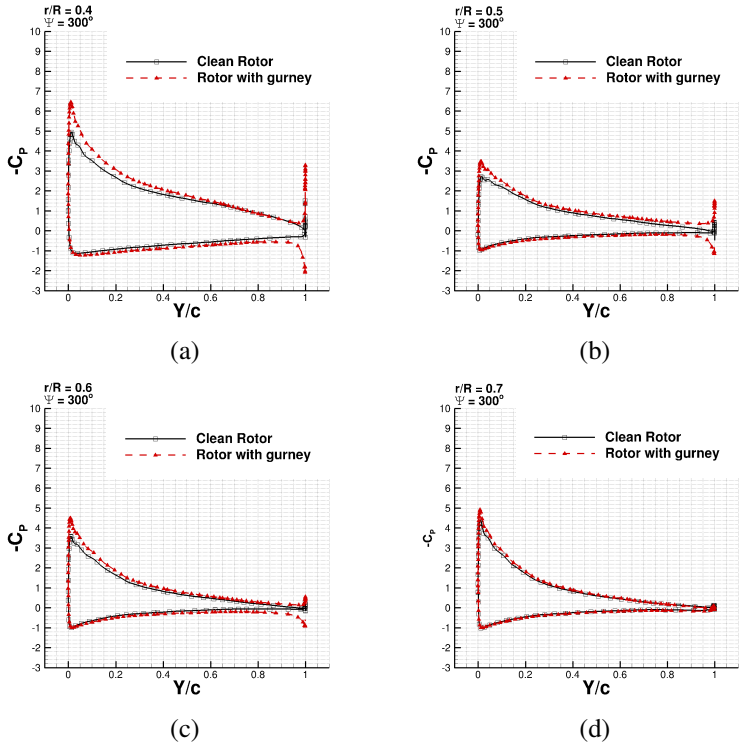

Figure 20: Surface pressure coefficient at $r/R = 0.4$ (a), $r/R = 0.5$ (b), $r/R = 0.6$ (c), and $r/R = 0.7$ (d) of the approximate W3 Sokol blade at azimuth $\Psi = 300^o$ at forward flight. Case conditions are presented in Table 1.

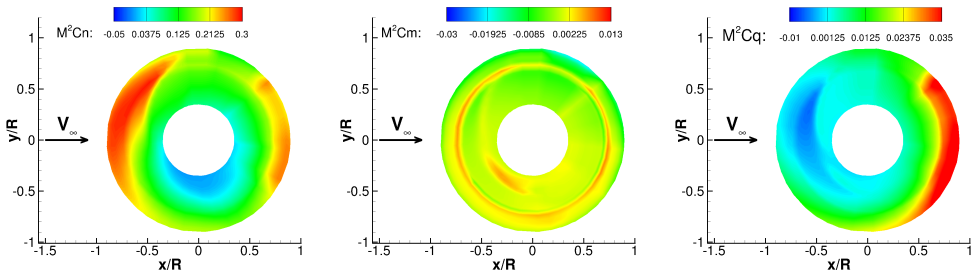

Figure 21: (a) Normal force, (b) Pitching moment, and (c) Torque coeffiecient of the clean rigid W3 Sokol MR. Forward flight conditions are presented in Table 1.

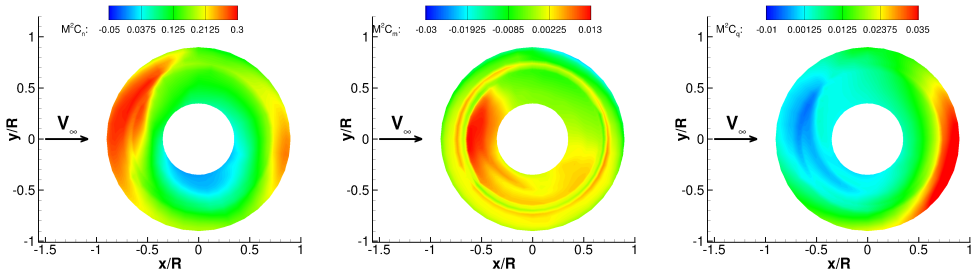

Figure 22: (a) Normal force, (b) Pitching moment, and (c) Torque coeffiecient of the rigid W3 Sokol MR with active gurney flap. Forward flight conditions are presented in Table 1.

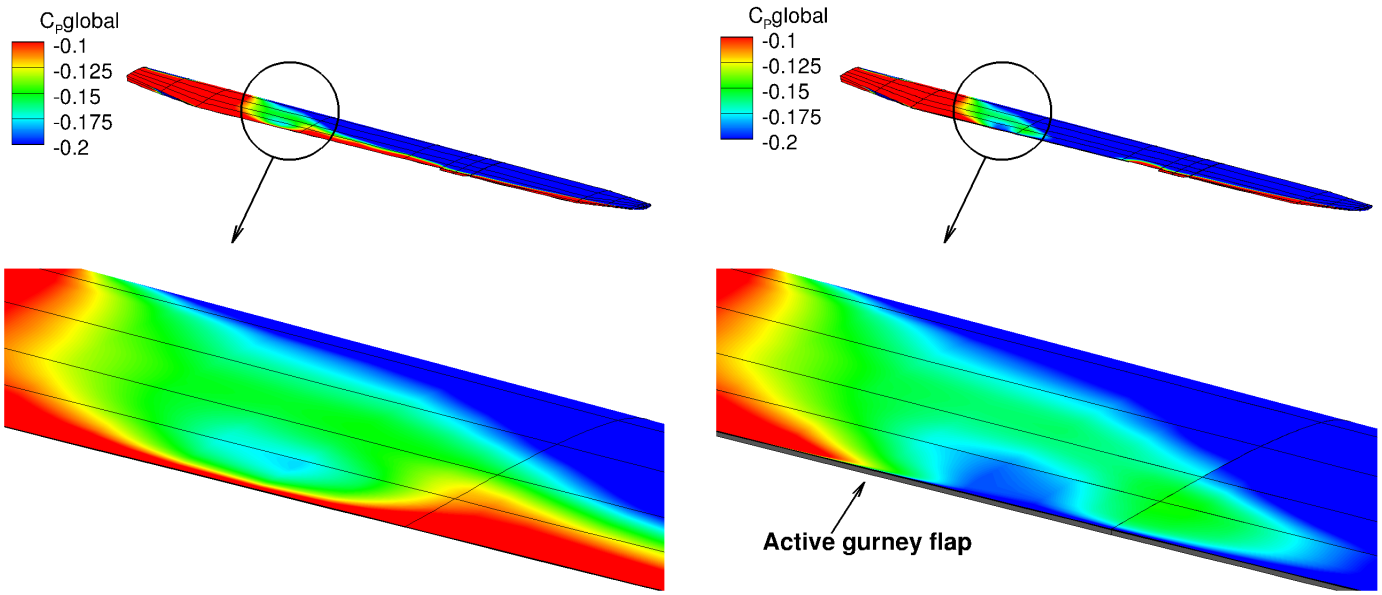

(a) (b)

Figure 23: Negative surface pressure coefficient based on the freestream velocity on clean blade (a), and (b) blade with active gurney flap (2% chord) at $\Psi = 290^o$. W3 Sokol MR in forward flight. Case are presented in Table 1.

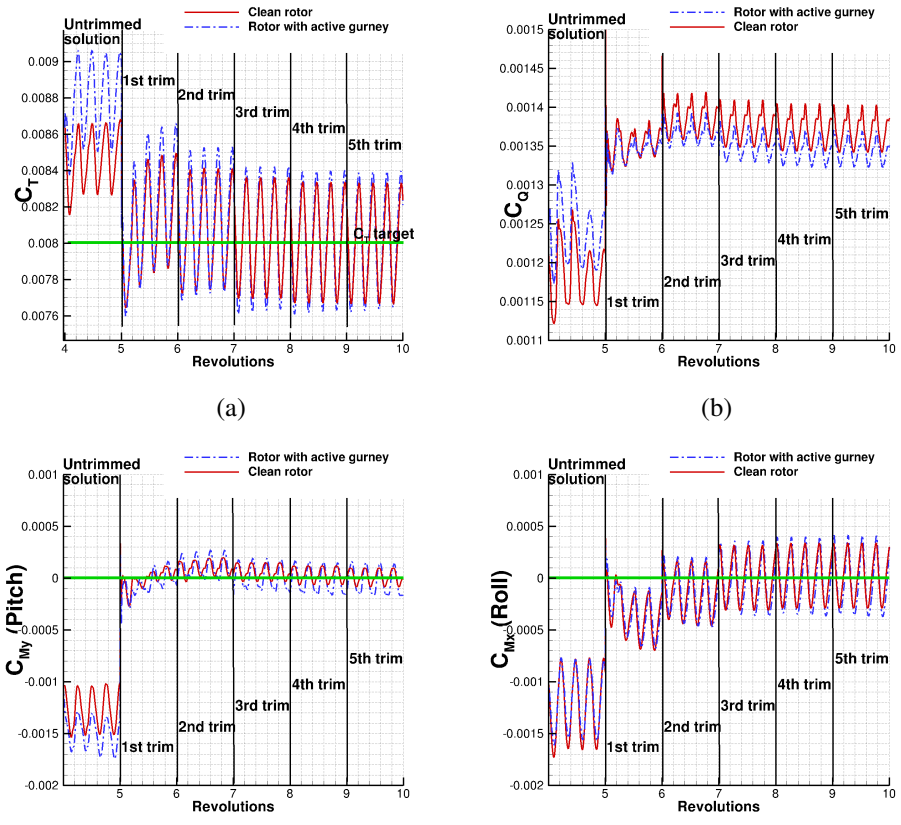

(a) (b)

(c) (d)

Figure 24: Trimming history of (a) thrust, (b) torque, (c) rotor disk pitching momnent, and (d) rotor disk rolling moment of the W3 Sokol MR in forward flight. Flight conditions are presented in Table 1.

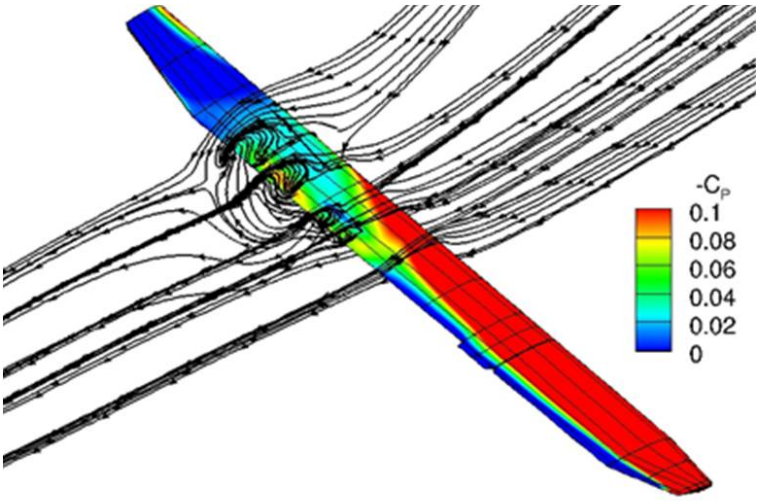

(a)

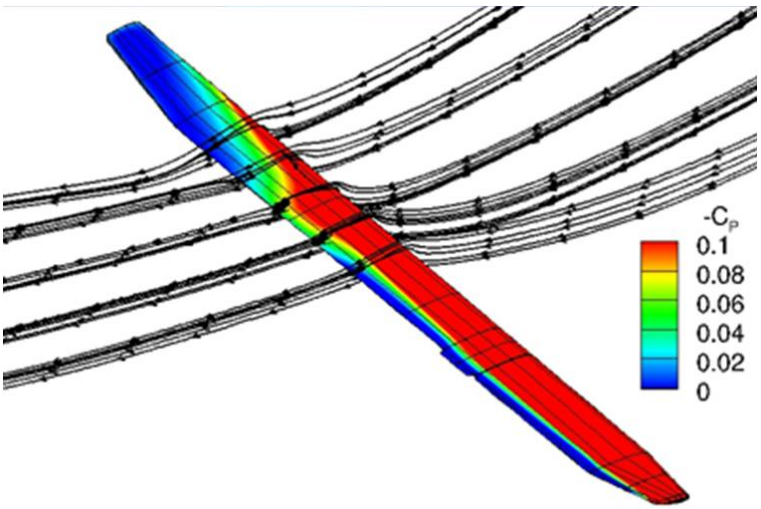

(b)

Figure 25: Visualization of the separated flow for (a) the clean blade and (b) the blade with an active gurney of $0.02c$ at $\Psi = 270^o$ of the W3 Sokol MR in forward flight. Case conditions are presented in Table 1.